



Research paper

Acoustic emission for the prediction of processing regimes in Laser Powder Bed Fusion, and the generation of processing maps

Rita Drissi-Daoudi^{a,*}, Giulio Masinelli^b, Charlotte de Formanoir^a, Kilian Wasmer^b, Jamasp Jhabvala^a, Roland E. Logé^a

^a Thermomechanical Metallurgy Laboratory – PX Group Chair, Ecole Polytechnique Fédérale de Lausanne (EPFL), Neuchâtel, Switzerland

^b Laboratory for Advanced Materials Processing (LAMP), Swiss Federal Laboratories for Materials Science and Technology (Empa), Thun, Switzerland

ARTICLE INFO

Keywords:

Laser Powder Bed Fusion
Acoustic monitoring
Convolution neural networks
Generalization
Robustness
Processing maps

ABSTRACT

The Laser Powder Bed Fusion (LPBF) process is of high interest to many industries, such as motors and vehicles, robotics, biomedical applications, aerospace, and others. LPBF workpieces can indeed achieve near full density and high resistance. However, a large amount of pore formation, in conjunction with the probabilistic nature of defect formation, results in a lack of process repeatability and reproducibility. This limits the range of industrial applications requiring high quality and defect free workpieces. To overcome this issue, we developed an acoustic monitoring system able to classify with high confidence three processing regimes (*lack of fusion pores*, *conduction mode*, *keyhole pores*) using a Convolution Neural Network (CNN). For the first time, we infer the processing regime based on AE waves produced during the LPBF process for conditions that are new and not part of the training database (>96%). The choice of processing conditions used in the database (training sets) is discussed in details, looking at the influence of their number, relative normalized distance, and position in the processing map on the classification accuracy. We found that the higher the number of processing conditions in the database, the higher the classification accuracies. Moreover, the higher the relative normalized “distance” between training and testing sets (measured in terms of laser speed and power), the lower the classification accuracies. Finally, the threshold defining the minimum number of training processing conditions is identified as eight to obtain a robust model able to identify the processing regimes for new laser parameters within the processing map. This number can be lowered to six if the training sets are in the surrounding region of the testing set. When one process parameter (speed, power, or normalized enthalpy) is constant between all the training and the testing sets, only four parameter sets allow a high classification accuracy (>88%). These results demonstrate the potential of in situ acoustic emission for monitoring the additive manufacturing process, in particular when the process conditions may deviate from the conduction mode. Finally, for a well-chosen set of training conditions, the model is able to construct a full processing map without additional experiments.

1. Introduction

In the past years, additive manufacturing (AM) has brought a new paradigm in the production of metallic parts, allowing the design of complex and intricate geometries while minimizing both lead time and buy-to-fly ratios [1]. Among the various categories of AM processes, Laser Powder Bed Fusion (LPBF), also known as Selective Laser Melting (SLM), consists in building up successive layers of pre-alloyed metallic powder according to a predefined 3D CAD model by selectively melting each layer of powder with a high-power laser beam [5–8]. Although this technology has gained significant interest from many industries [2–8]

due to its versatility and accuracy, a number of drawbacks still limit its range of applications and impede a wider industrial use [9–13].

In particular, LPBF suffers from a frequent and sometimes hard-to-predict formation of defects, such as pores, which impedes certification processes. Porosity in as-built LPBF parts can originate from multiple causes, including the quality of the powder feedstock and the laser-material interactions. This latter source includes lack-of-fusion and keyhole pores. Lack-of-fusion pores result from an insufficient energy input, inducing incomplete melting of the powder during laser processing [14–17]. On the other hand, keyhole pores are caused by an excessive heat input: vaporization of the metal creates a deep

* Corresponding author.

E-mail address: rita.drissidaoudi@gmail.com (R. Drissi-Daoudi).

<https://doi.org/10.1016/j.addma.2023.103484>

Received 6 October 2022; Received in revised form 26 February 2023; Accepted 5 March 2023

Available online 7 March 2023

2214-8604/© 2023 The Author(s). Published by Elsevier B.V. This is an open access article under the CC BY license (<http://creativecommons.org/licenses/by/4.0/>).

keyhole-shaped depression zone whose collapse can generate a void in the lower region of the melt pool [18–23]. Optimal conditions for minimal porosity content are encountered in the conduction mode, a transition regime between lack-of-fusion and keyhole [23,24].

Different tools have been developed to determine and thus mitigate the occurrence of pores. For a given material, processing maps based on parameters such as laser power and speed can be built to find the optimum conditions for high-density parts [24–28]. However, establishing such 2D-processing maps is a laborious procedure, requiring extensive printing of specimens using a variety of process parameters followed by a very time-consuming metallurgical characterization of the as-built parts. Furthermore, this trial-and-error process optimization needs to be reiterated when transitioning from either one alloy [29], or one LPBF machine, to another.

In most laser processes dealing with powders, the laser-material interaction is highly non-linear and always exhibits a non-negligible stochastic component. This leads to non-reproducibility of microstructures and properties, and non-homogeneity of the printed parts. Moreover, the generation of unpredictable spatter [30–35] and contamination leads to irregular defect formation [12]. In order to detect the formation of defects during the LPBF process, and identify the melting regime (lack-of-fusion, conduction, or keyhole), real-time process monitoring is a promising solution/approach. In the past 10 years, various optical techniques have been investigated, including spatially integrated sensors such as photodiodes [36–38], pyrometers [39–43], infrared and high speed cameras [36,37,41,43,44]. Complementary to these optical techniques, acoustic emission (AE) has been reported as a high sensitivity, low-cost and robust technique for monitoring laser processes.

The analysis of AE was first identified as a valid technique for monitoring laser welding [45–48]. One drawback of the AE sensors is that they record any AE waves produced during the laser processes, including the undesired noise from the machine or the environment [38, 49,50]. Consequently, it is not a trivial task to isolate the AE information coming from the laser-material interactions [51]. To address this issue, state-of-the-art machine learning algorithms were able to classify welds of various regimes and quality based AE signals [50,52–55]. More recently, the potential of AE as a monitoring tool has been extended to the field of laser-based additive manufacturing. Several papers have demonstrated the ability to differentiate lack-of-fusion, conduction, and keyhole regimes with high confidence, based on AE signal analysis [29, 49,56–67].

To be specific, over the past few years, Convolutional Neural Networks (CNN) have become a common algorithm for acoustic classification tasks [29,56], demonstrating great effectiveness and enabling the possibility of suppressing stationary noise. For example, Shevchik et al. [56] used a Fiber Bragg Grating (FBG) as AE sensor, and combined two types of CNN (a Spectral one and a conventional one). They have successfully classified the quality of LPBF with a classification accuracy around 80%. In a following work, Shevchik et al. [62] used two running windows with various time span as input to several types of CNNs, to address the localization of defects. The classification accuracies varied between 73% and 91%, depending on the time span of the running window and the process quality. Similarly, Ye et al. [63] used a deep belief network to classify acoustic data of five category – balling, slight balling, normal, slight overheating, overheating – with high accuracy (95%) in the LPBF process. Eschner et al. [61] have designed a Neural Network to classify three density classes of laser operation with 90% accuracy. Drissi-Daoudi et al. [29] have compared four ML algorithms (Logistic Regression, Random Forest, Support Vector Machine and a CNN) for the classification of three process regimes (*keyhole pores*, *conduction mode* and *LoF pores*) for three different alloys (stainless steel, bronze, and Inconel), using a low cost airborne AE sensor. All algorithms had comparable and high classification accuracies (around 90%), for all alloys. The authors selected two process parameters per regimes, with specific normalized enthalpy, to prove that the extracted AE features

used for training the ML algorithms relate to the laser-material interaction. Finally, they designed a CNN capable of simultaneously classifying the alloy and the process regime.

Tempelman et al. [64] used a Support Vector Machine (SVM) to detect keyhole and non-pore segments of single lines using process parameters scattered in the 2D processing map. The data segmentation and labeling were obtained by X-ray tomography. Their approach confirmed the previous works from Shevchik et al. [29,62] that keyhole pore formation can be detected using airborne AE sensors combined with ML algorithms. However, in all AE-based studies for LPBF, the techniques' performance was evaluated on random AE signals that are, obviously, not part of the training database but coming from the collected database using the same parameters set; which raises two questions. First, does the ML algorithm classify the process parameters or the laser-material interaction? Clearly, the main goal is to monitor the laser-material interaction leading to the different process regimes (LoF, conduction, and keyhole) and not the process parameters themselves; otherwise, we would just extract this information from the machine directly. The second question is the ability of the ML algorithm to classify AE signals from trained process regimes but from new (unseen) parameter sets. This generalization of the ML predictability is a critical step towards AE based process monitoring. Finally, significant factors and exhaustive details for constructing a robust database are overall lacking in the literature. Consequently, the novelty of this contribution is twofold. First, it focuses on the ability of ML algorithms to classify AE data outside the parameters sets they were trained on. Second, the present study provides all the necessary tools to help building an otherwise time-consuming processing map for a given alloy.

The present work studies the classification of AE signals recorded by a microphone during LPBF of a 316 L stainless steel alloy. The occurrence of three process regimes (*keyhole pores*, *conduction mode* and *LoF pores*) is identified through metallurgical characterization. The CNN algorithms are trained with three categories representing the three different process regimes; as well as with the background noise as the fourth category, i. e., the noise of the machine and process when the laser is off. A CNN is selected for the classification tasks of these four categories.

The paper is organized into 4 Sections. Section 2 details the method and experimental plan, while Section 3 presents the results and discussion. The generalization of the CNN model, trained with twelve parameter sets, is tested on an unseen thirteenth parameter set. We check in what extent the accuracy of the classification relates to: (i) the position (in the 2D space) and number of the parameter sets used in the training database with respect to the tested set, (ii) the influence of key process parameters – normalized enthalpy, laser power and speed, (iii) the relative normalized “distance” in terms of power, speed and normalized enthalpy between the training and the tested set. The results provide insights into the collection of a robust model for classification of LPBF processing regimes based on AE, which are summarized in the conclusion.

2. LPBF experiments

2.1. Experimental setup and data acquisition

All experiments of this work were performed on an in-house LPBF system shown in Fig. 1. The customized LPBF contains a hopper filled with powder that deposits each layer by gravity when the piston below the substrate moves down by the required layer thickness. A continuous-wave (CW) modulated Ytterbium fiber laser is used for melting the powder. The fiber laser operates in a continuous mode with a 1070 ± 10 nm wavelength and a maximum power of 500 W. The beam diameter is around $42 \mu\text{m}$ ($1/e^2$) at the focal plane with $M^2 < 1.1$. The laser scan speed is up to $20 \text{ m}\cdot\text{s}^{-1}$. The chamber's atmosphere is controlled under a laminar flow of argon and a monitored oxygen level of maximum 200 ppm. The build chamber is equipped with a CM16/CMPA40–5 V ultrasound microphone (Avisoft Bioacoustics), as shown in Fig. 1 (6). This

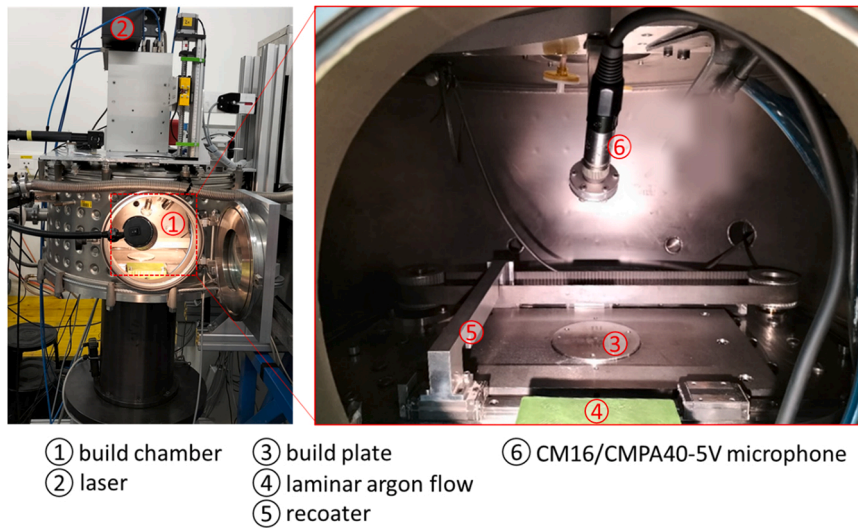


Fig. 1. Experimental set-up of the custom-built LPBF with the CM16 microphone.

main advantage of this microphone is that it has a flat response up to 200 kHz. It is positioned on the top of the build chamber so that the recording face points to the process zone while not disturbing the deposition system and being protected from powder, spatters, and fumes. It is placed at a distance of approximately 23 cm from the center of the substrate. An Advantech Data Acquisition (DAQ) card (Advantech, Taiwan) records the output from the microphone. The AE signals are acquired at a rate of 0.6 MHz and stored locally for processing with a custom-built C# code that interacts with the Advantech DAQ card. The data acquisition rate was chosen to ensure that the Nyquist Shannon theorem [68] is satisfied. The data acquisition is triggered by the laser head signal. This ensures synchronization between the LPBF process and the obtained data.

All experiments were performed with a stainless steel MetcoAdd 316 L micro powder (Oerlikon Metco) with a particle size distribution between 15 and 45 μm . Its composition is presented in Table 1 and the corresponding physical and optical properties are given in Table 2. The final composition of the LPBF fabricated samples may slightly differ as a result of the evaporation of the most volatile elements, such as carbon, silicon, and phosphorus. The absorptivity α (Table 2) of the powder was experimentally measured with a Perkin Elmer Lambda 900 spectrophotometer for wavelengths from 900 to 1'200 nm and a layer thickness of 40 μm . Fig. 2 presents an SEM image of the powder used to fabricate the samples.

2.2. Experimental plan

We considered three distinct process regimes: *LoF pores*, *conduction mode*, and *keyhole pores*. For each regime, thirteen cubes of $13 \times 13 \times 3 \text{ mm}^3$ with thirteen different parameter sets were printed. The thirteen process parameters are given in Table 3 and plotted in Fig. 5. 1-mm-thick porous structures were built on top of the base plate as support for the samples in order to ensure that the experiments would have the same heat flow as when processing bulk material. On top of these support structures, high-density layers were built over 2 mm to guarantee similar initial conditions for all experiments. Finally, for each of the three above-mentioned process regimes, 10 layers (above the red line in Fig. 4 and schematically in Fig. 3) of 110 overlapping line tracks were

Table 1

Chemical composition of stainless steel (316 L) powder (weight fraction %).

Fe	Cr	Ni	Mo	Other	C
Balance	18	12	2	< 1.00	< 0.03

Table 2

Physical and optical properties of stainless steel 316 L.

	Parameters values
Absorptivity α [-]	0.52
Density ρ [kg/m^3]	7'900[70]
Specific heat C [$\text{J}/\text{kg.K}$]	490[70]
Melting point [K]	1'640[70]
Latent heat of melting L_m [kJ/kg]	260[70]
Laser spot radius [μm]	42
Thermal diffusivity [m^2/s]	$3.5 \cdot 10^{-6}$ [70]

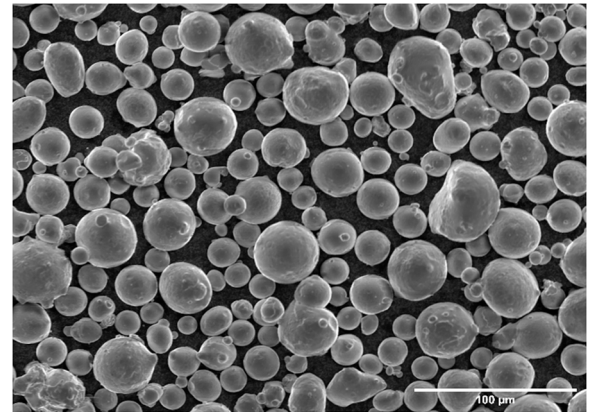


Fig. 2. SEM picture of the SS 316 L powder used.

produced, during which the AE signals were recorded with the microphone. The scanning strategy was unidirectional and parallel, with a hatch distance of 0.1 mm and a layer thickness of 40 μm (Fig. 3). The hatch spacing and layer thickness are critical factors for defect formation, but for the purpose of this study, they were kept constant. The unidirectional parallel scanning strategy was adopted for ease of acoustic signal acquisition. The hatch distance and layer thickness were selected to be consistent with the laser beam size while still enabling the formation of the three regimes studied. Fig. 3 presents a schematic of the built samples and their dimensions.

For all 39 cubes, the data labeling of the process regime was identified via cross-section analysis, and a metallography analysis was performed on all of the samples. Typical examples of the microstructure for each process regime are presented in Fig. 4. The micrographs of the four

Table 3

Process parameters (power, speed, and normalized enthalpy) used for the experimental plan for the three categories, *keyhole pores*, *conduction mode*, and *LoF pores*. The values in bold are iso-speed, iso-power, and iso-normalized enthalpy for each category. The sample n°13 in *Italics Bold* is the black central point in Fig. 5, common for the three iso-parameters.

N°	<i>Keyhole pores</i>			<i>Conduction mode</i>			<i>LoF pores</i>		
	Power [W]	Speed [mm/s]	Normalized enthalpy [-]	Power [W]	Speed [mm/s]	Normalized enthalpy [-]	Power [W]	Speed [mm/s]	Normalized enthalpy [-]
1	282	350	89.9	107	450	30.1	68	450	19.1
2	267	350	85.1	96	450	27.0	64	450	18.0
3	235	350	74.9	82	450	23.1	57	450	16.0
4	220	350	70.1	71	450	19.9	51	450	14.3
5	251	276	90.1	89	350	28.4	61	358	19.2
6	251	310	85.0	89	400	26.5	61	400	18.2
7	251	398	75.1	89	500	23.7	61	500	16.3
8	251	457	70.0	89	550	22.7	61	550	15.5
9	240	320	80.0	85	410	25.0	59	430	17.0
10	245	333	80.1	87	432	25.0	60	443	17.0
11	256	364	80.0	91	466	25.1	61	457	17.0
12	261	378	80.1	93	490	25.0	62	470	17.1
13	251	350	80.0	89	450	25.0	61	450	17.1

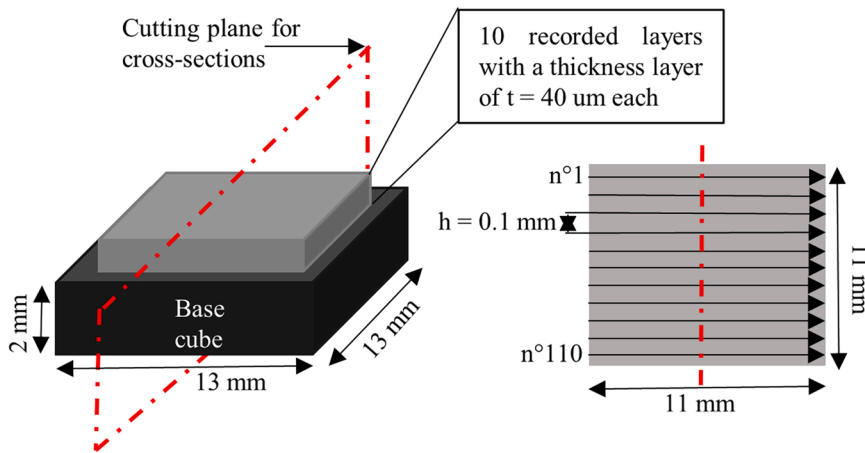


Fig. 3. A schematic of the printing of samples and their dimensions. High-density layers were first built over 2 mm (black cube) to establish repeatable initial conditions for all experiments. For each of the three process regimes, 10 layers of 110 overlapping line tracks were then produced, during which the AE signals were recorded with the microphone. The scanning strategy was unidirectional and parallel, with a hatch distance of 0.1 mm and a layer thickness of 40 μm . The red plane represents the cutting plane for cross-sections.

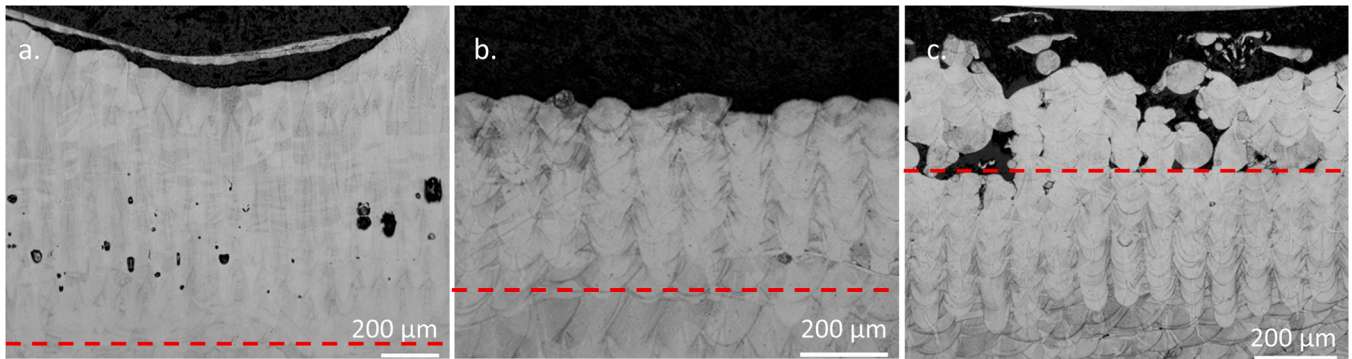


Fig. 4. A typical example of the microstructure of the three regimes. a. *keyhole pores*, b. *conduction mode*, c. *LoF pores*. The dotted red line delimits the recorded lines from the printed cube.

extremes parameters samples (samples 1, 4, 5, and 8, presented in Fig. 5) are presented in the [supplementary materials](#).

The samples were etched with diluted Aqua regia (100 ML HNO_3 , 100 ML HCl , 100 ML H_2O) for 30 s to reveal the microstructure and melt pool morphology. Micrographs were taken with a Leica DM6000M light optical microscope in bright field mode.

As illustrated in Fig. 5, the process parameters were chosen to have, for each process regime, five sets of parameters with iso-power ($P = 61$ W, $P = 89$ W, and $P = 251$ W), five with iso-speed

($v = 350$ mm/s or $v = 450$ mm/s), and five with iso-normalized enthalpy ($\Delta H = 17$, $\Delta H = 25$ or $\Delta H = 80$).

The normalized enthalpy ΔH is defined as [24,69]:

$$\overline{\Delta H} = \frac{\alpha P}{\rho(C\Delta T + L_m)\sqrt{\pi\omega^3 VD}} \quad (1)$$

Where α is the absorptivity of the powder layer, as defined in reference [24], P is the laser power (W), ρ the density (kg/m^3), C the specific heat (J/kg.K), ΔT the difference between the melting and initial temperature

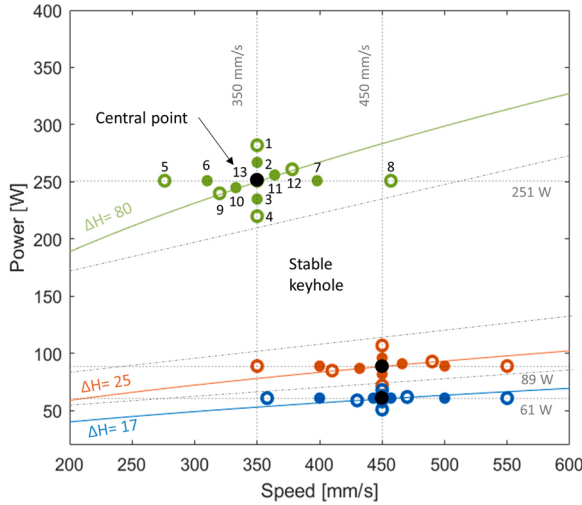


Fig. 5. Process parameter map with the thirteen parameter sets for each category, in green for the *keyhole pores* domain, in orange for the *conduction mode*, and in blue for *LoF pores*. The parameter sets are numbered from 1 to 13 for the *keyhole pores* domain. The same numbering strategy can be transferred to the two other domains. The “central point” is depicted in black. Three iso-normalized enthalpies at 80, 25, and 17 are plotted. The full markers are the six parameter sets closest to each central point, and the six empty markers are the six parameter sets the furthest away from the central points.

(K), L_m the latent heat of melting (kJ/kg), ω the laser spot radius (m), v the laser speed (m/s), D the thermal diffusivity (m^2/s).

All three iso-conditions share a common central point (in black in Fig. 5) corresponding to line n°13 in Table 3, which leads to a total of thirteen experiments for each regime. The enumeration in Fig. 5, given for the *keyhole regime*, is transferable to the two other process regimes (Table 3).

The DoE is designed such as to allow predicting the process regime with an unseen parameter set (central point, n° 13) with the training performed on a database composed of 12 parameter sets surrounding it. It also allows predicting the process regimes related to parameter sets that are off-centered (n° 1, 4, 5, and 8) with 12 parameter sets that are further away in the processing map.

The boundaries in grey in Fig. 5 are for illustrative purposes only. Although the normalized enthalpies provided a starting point for the DoE parameters, the actual boundaries were determined through experimental analysis using cross-section and metallography techniques on all samples. The influence of the “distance” (in the processing map) between the data points used for the training and the prediction will be studied by comparing the results of the classification when the database is formed with the 6 closest points (full markers in Fig. 5, n° 2, 3, 6, 7, 10, 11) to the results when the training is based on the 6 other more distant points (empty markers in Fig. 5, n° 1, 4, 5, 8, 9, 12). Moreover, the prediction of the central point process regime will be tested with three databases trained with the 4 parameter sets in iso-power, iso-speed, or iso-normalized enthalpy, respectively, in order to highlight the influence of the choice of process parameters on the training. Finally, the influence of the relative normalized “distance” in terms of normalized enthalpy, power, and speed, as well as the number of parameter sets needed for a high-confidence prediction of an unseen point, will be determined. The relative normalized “distance” in terms of normalized power is defined in Eq. (2).

$$d_p = \frac{\sum_{i=1}^n (P_{\text{training}} - P_{\text{unseen}})}{\sum_{i=1}^n P_{\text{training}}} \bullet 100[\%] \quad (2)$$

where n is the number of parameter sets in the training database, P_{training} the power [W] of each set in the training database, and P_{unseen} the power

[W] of the unseen parameter set. The same definition can be applied to d_s and $d_{\Delta E}$, by considering the laser speed values and the normalized enthalpy values, respectively.

A one-second delay was applied between each line track to ensure that the recording of each line was performed under the same thermal conditions. Moreover, this delay guarantees that the reverberation of the sound inside the build chamber, which can last ~ 100 ms after the laser stops, is completely attenuated. Again, this guarantees that the recording of a new line always starts under the same conditions [71]. However, compared to the processing maps reported by Tucho et al. [25], the one-second delaying time reduces the size of the conduction regime domain and, even more significantly, the one of the LoF regime. In contrast, the stable keyhole regime domain (i.e., with no porosity formation) becomes larger.

2.3. Data processing

A pre-delay of 0.5 ms is implemented to make sure that the acoustic signal is recorded from the beginning of the laser process. To ensure having recorded the signal over the entire line, 27'000 data points were acquired for the *keyhole pores* process regimes, 21'000 for the *conduction mode*, and 18'000 for the *LoF pores*. All acoustics signals were then extracted as follows: the first 3'000 points were removed, the next 10'000 points were kept, and the remaining points were also removed. With this procedure, all analyzed signals have the same length, and the non-steady state conditions (when the laser has not yet reached the required speed) are excluded from the analysis.

A CNN is chosen for the classification tasks. CNNs have been proven to be effective for noisy signals [29,62], and they avoid the feature extraction step. It is implemented using the PyTorch library, chosen for the classification tasks. The AE signals have been filtered with a low pass filter at 60 kHz, as the microphone is polarized for higher frequencies, and because [29] showed that the information responsible for the three regimes formation where mostly below 40 kHz. The signals were then downsampled by a factor of four, and finally normalized between 0 and 1.

For all signals, spectrograms, after the post-processing, were extracted from the acoustics signals. A short window increases the time and spatial resolution of defect detection, but could be more affected by noise. The time span must also be large enough for at least one defect to form. A good compromise was obtained with a window of 16 ms (10'000 data points). In order to have the best tradeoff between the resolution in time and in frequency, a spectrogram of size 97×626 was selected after an exhaustive search. A typical spectrogram for each process regime is presented in Fig. 6. Visualizing patterns in the spectrograms may be challenging for humans, which is why we proposed using CNNs to extract relevant features from the spectrograms. CNNs are prone to overfitting, and without proper data management, the results might be overly optimistic. To address this issue, we took several measures, including using a large dataset, carefully separating the training and testing data.

1'100 acoustics signals were taken per sample. As a result, if twelve parameter sets (samples) are included in the training set, then 13'200 signals (and thus the same amount of spectrograms) are considered per category.

The training of the CNN is performed on 80% of the signals (randomly picked), and the remaining 20% of the signals are kept for the validation of the model's performance. The model is then tested on 1100 signals from the same process regime or category but with another parameter set unseen by the algorithm. This temporal split approach is utilized to further improve the model's generalization capabilities. AE signals have a temporal component, indicating that signals generated during a specific period may share common features or characteristics. By splitting the dataset based on the time of data acquisition — by printing the test samples after the training ones — we ensured that the model was trained on a diverse range of features over time, which can

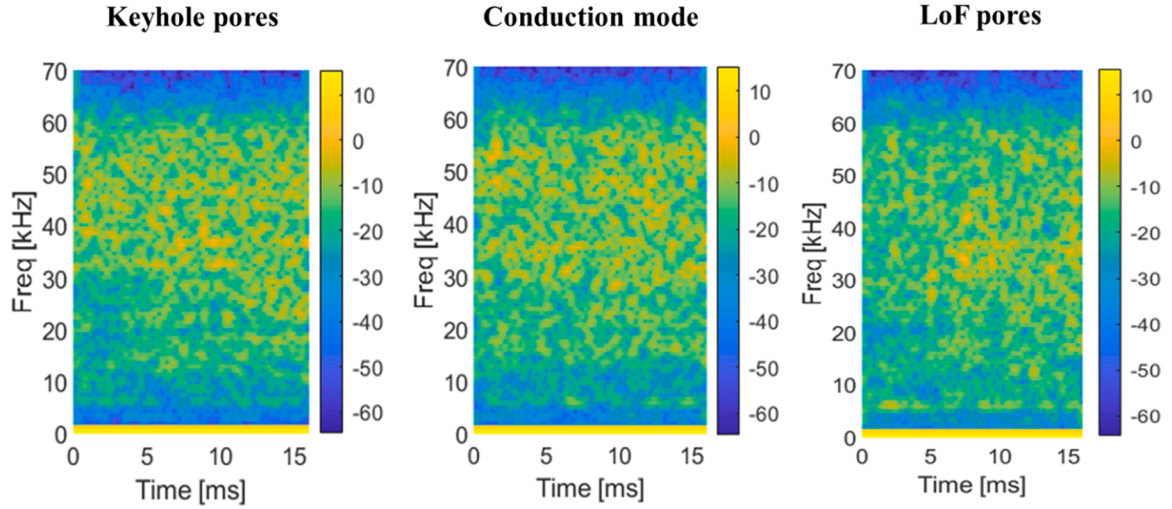


Fig. 6. Example of a spectrogram for the three regime related categories.

improve its ability to generalize to new data. Additionally, using a temporal split helps simulate a more realistic setting where the model is tested on data that has not been seen before. This approach mimics the real-world scenario where the model is trained on historical data and used to make predictions on new data. The CNN architecture is illustrated in Fig. 7. It includes two 2D convolution layers max pooled by 2×2 ; each batch-normalized to avoid overfitting as well. The Rectified Linear Units (ReLU) activation function is applied to both layers. Two fully connected layers are following these layers. The model is trained for 50 epochs with a batch size of 1000, a learning rate of $5e-4$, and the Adam optimizer. The same architecture is kept unaltered for all the classifications in this work for comparison purposes. The use of background noise in training is only to help the algorithm. The classification accuracy for the background noise was always 100%. Hence, it will not be further mentioned in the description of this work.

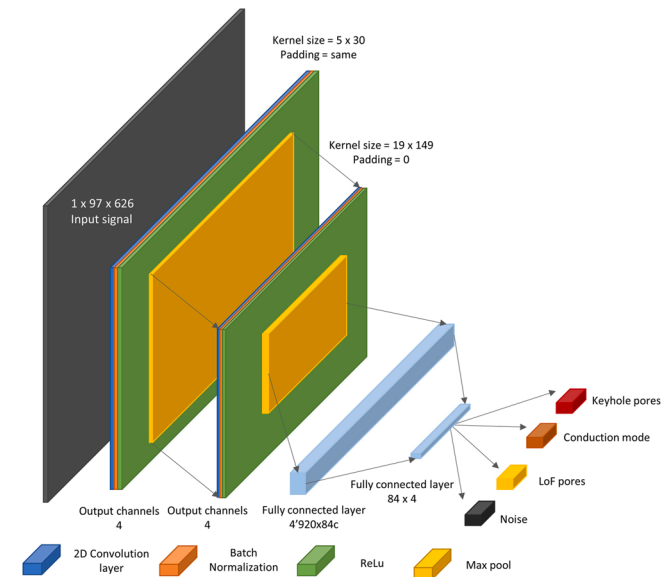


Fig. 7. Scheme of the CNN architecture with two convolutional layers and two fully connected layers.

3. Results and discussion

3.1. Toward the generalization of the ML model over the entire processing map

One important objective of this paper is to investigate to what extent the proposed ML algorithm can predict the process regime of an unseen parameter set (i.e., not part of the training) from its recorded AE signals.

As already described in Section 2.2, the airborne AE signals from a chosen number of parameter sets are used for training the ML, which is then tested on a new parameter set. In this work, the CNN architecture in Fig. 5 has been trained first with twelve parameter sets (experiments n°1–12 in Fig. 3 and Table 3) for each process regime (*LoF pores*, *conduction mode*, and *keyhole pores*). Then, the model was tested by classifying the process regime on an unseen parameter set (black point in Fig. 5, n°13 in Table 3). As shown in Fig. 3, the unseen parameter is surrounded by the ones used for training the ML model.

The results of the classification accuracies for the three process regimes (*LoF pores*, *conduction mode*, and *keyhole pores*) are given in the confusion matrix Table 4.

The algorithm was tested on 1/100 signals acquired when all samples 13 were fabricated (for the three regimes). True positive classification is defined as when the model recognizes the test signal to belong to the correct category. Conversely, a false negative occurs when the signal is classified as belonging to another category, while a false positive occurs in the detected category. The accuracy, expressed as a percentage and represented by the diagonal values in Table 4, is calculated as the number of true positives divided by the total number of tests in each category. The misclassifications, including false positives and false negatives, are represented by the number of such occurrences divided by the total number of tests in each category. As an example, in Table 4, the *keyhole pores* tested signals were accurately classified as *keyhole pores* with a high accuracy rate of 96%, while 2% were classified as *conduction mode* and 2% as *LoF pores*. From this table, it is observed that classification results are higher than 96% for all three categories. We can therefore conclude that the model can be generalized to predict, with high confidence, the regime of a new, unseen parameter set if it is surrounded (in the processing map) by parameter sets used to train the algorithm. The generalization here can be thought of as a type of interpolation.

Table 4

Confusion matrix for a CNN model trained on 12 parameter sets and tested on an unseen 13th parameter set.

Ground truth \ Classification accuracy [%]	Keyhole pores	Conduction mode	LoF pores
Keyhole pores	96	2	0
Conduction mode	2	96	0
LoF pores	2	2	100

3.2. Influence of the position, number of parameter sets and choice of process parameters on the classification accuracy

While the previous sub-section demonstrated the interpolation abilities of our CNN algorithm, the present section investigates the influence of different factors on the classification accuracy of the tested parameter sets to establish the conditions required to construct a robust model.

For each process regime, the factors considered to influence the classification accuracy are:

- The position (in the processing map) of the parameter sets chosen for the training database as compared to the tested (unseen) parameter set.
- The number of sets in the training database
- The influence of the chosen process parameters: laser power, laser speed, and normalized enthalpy.

- The relative normalized “distance” in terms of laser power, laser speed, and normalized enthalpy (d_p , d_s and $d_{\Delta E}$) between the average values of the parameter sets considered in training and the tested (unseen) parameter set.

The same CNN architecture (Fig. 6) is used.

3.2.1. Influence of the position of the parameter sets in the training database with respect to the tested (unseen) parameter set

To study the influence of the position of the training parameter sets with respect to the unseen parameter set, the four extreme parameter sets (n° 1, 4, 5, and 8 in Fig. 3 and Table 3), in terms of laser power and speed, are successively chosen as the unseen parameter set. The remaining 12 other parameter sets are, each time, used for training the ML. Table 5 shows the corresponding 3-by-3 confusion matrices for the classification of the three regimes. The unseen parameter set has either the highest speed (n°8, Table 5 a.), the highest power (n° 1, Table 5 b.), the lowest speed (n°5, Table 5 c.), or the lowest power (n°4, Table 5 d.).

Table 5

Confusion matrices for CNN models trained with twelve parameter sets and tested on the a. highest speed set, b. highest power set, c. lowest speed set, and d. lowest power set.

a. Highest speed set				b. Highest power set			
Ground truth \ Classification accuracy [%]	Keyhole pores	Conduction mode	LoF pores	Ground truth \ Classification accuracy [%]	Keyhole pores	Conduction mode	LoF pores
Keyhole pores	83	15	4	Keyhole pores	97	9	3
Conduction mode	6	84	1	Conduction mode	2	90	1
LoF pores	1	1	95	LoF pores	1	1	96

c. Lower speed set				d. Lower power set			
Ground truth \ Classification accuracy [%]	Keyhole pores	Conduction mode	LoF pores	Ground truth \ Classification accuracy [%]	Keyhole pores	Conduction mode	LoF pores
Keyhole pores	96	1	3	Keyhole pores	98	17	4
Conduction mode	3	99	2	Conduction mode	2	75	1
LoF pores	1	0	95	LoF pores	0	8	95

Overall, it can be seen that the classification accuracy remains high, although slightly lower values are obtained in *keyhole pores* and *conduction modes* for the “highest speed” unseen parameter set when compared to the earlier case for which the unseen parameter was the central black point (Table 4). However, the classification accuracy in conduction mode for the “lowest power” unseen parameter set, sample n°4, is significantly lower (75%). This decrease can be correlated to the fact that this set is located near the boundary between the *conduction mode* domain and the *LoF pores* domain (see Fig. 5). The micrographs of sample n°4 of the *conduction mode* and of sample n°1 of the *LoF mode* are displayed in Fig. 8.a. and Fig. 8.b., respectively. Although scattered *LoF pores* can be observed in Fig. 8.b., it can be seen that the microstructures are similar in terms of melt pool dimensions. The average melt pool depth and length for the *conduction mode* sample are equal to 63 μm and 87 μm , respectively. In the case of the *LoF pores* sample, they are 57 μm and 82 μm , respectively. In Ghasemi et al. [24], the minimum ratio between the melt pool depth and the layer thickness that guarantees the *conduction mode* state was reported to be around 1.5. This ratio is here equal to 1.57 and 1.43 in sample 4 (*conduction mode*) and sample 1 (*LoF pores mode*), respectively. It is possible that a low amount of *LoF pores* is present in sample 4 (*conduction mode*) while not visible in the analyzed cross-sections. The proximity between these microstructures could explain the decrease in classification accuracy for this sample set, as the AE signals are expected to have many similar features. This means that for a reliable and robust model, a local decrease in accuracy could be indicative of a parameter set located at the border between two processing regimes. In other words, it could help identify the frontiers of the processing regime domains when constructing a processing map.

3.2.2. The number of parameter sets

The influence of the number of sets in the training database was also evaluated. In addition to the 12 sets previously used (Table 3), training databases with six, eight, and ten different process parameter sets were employed. Once again, the trained CNN algorithm was used to predict the process regime of an unseen parameter set, chosen among the four most extreme points in the processing map (n°1, 4, 5, and 8 in Fig. 5). The parameter sets present in each training database were selected in order to maximize d_s and d_p . Similar to Table 5, Table 6 presents the 3-by-3 confusion matrices for the three categories (process regimes) on the four tested unseen conditions when ten, eight, and six parameter sets are included in the training database. The classification accuracies with ten parameter sets in the training database are similar to the ones obtained with twelve parameter sets (Table 5). The accuracies are high, except for the prediction of the unseen parameter set n°4, located at the border of the *conduction mode* domain. The lower accuracy can again be explained by this particular location, as discussed above, when using 12 parameter sets. The average classification accuracy for the models trained with 8 parameter sets is remarkably high for all tested unseen parameter sets. However, when six parameter sets are included in the training, the classification accuracies on unseen parameter sets are, on average, lower and more scattered, depending on the considered tested point. Six parameter sets do not seem to be sufficient to obtain a robust model able to perform accurate predictions in other unseen locations of the

processing map.

In addition to the number of parameter sets in the training database, the position of the sets with respect to the unseen parameter set was also considered. In the first case, the six sets with full markers (n° 2, 3, 6, 7, 10, 11) in Fig. 5 constitute the training database, and the model is applied for predicting the processing regime of the central point, n°13 (in black in Fig. 5). The accuracy results are compared with those obtained in the second case, i.e., when the six sets with empty markers (n° 1, 4, 5, 8, 9, 12) in Fig. 5 are in the training database, and the model is also applied on the unseen central point, n°13. In both cases, the average value of the process parameters considered in the training database are the same as for the unseen parameter set (both in terms of laser power and speed). However, the full marker sets are closer to the central point than the empty markers. It can be seen in Table 8 that all classification accuracies are very high (>91%) and that no significant difference between the two configurations can be noted.

From these results, it can be highlighted that the number of parameter sets in the training base can be lowered down to six if the points are surrounding the unseen parameter set. The average RMS “distance” in power (d_{p_RMS}) and in speed (d_{s_RMS}) between the training sets and the unseen parameter set is given in Table 7, considering either the closest or the most distant sets. Table 8.

$$d_{p_RMS} = \sqrt{\frac{1}{n} \sum_{i=1}^n (P_{training} - P_{unseen})^2} \quad (3)$$

The RMS distances (d_{p_RMS} , d_{s_RMS}) give us an evaluation of how far the training set is from the testing set. Where the normalized relative distances (d_s , d_p) give us an indication on how the training sets are distributed around the tested set.

The model has a good classification accuracy both when the sets are close to the unseen set (small d_{p_RMS} and d_{s_RMS} values as shown in Table 7) as when the sets are more distant from the tested set. Therefore, the parameters that seem to have a higher importance are the relative normalized distances.

3.2.3. The process parameters: speed, power, normalized enthalpy

The influence of the choice of process parameters in the training set was also studied. The processing map is expressed in terms of laser speed and power. The normalized enthalpy (Eq. 1) is a function of these two process parameters. In each process regime, the four-parameter sets with the same speed (i.e., “iso-speed” parameter sets, n°1, 2, 3, 4 in Fig. 3) were chosen to compose the training database, and the trained CNN was used for predicting the process regime of the central unseen parameter set (n° 13). The same strategy was used with the four “iso-power” (n° 5, 6, 7, 8 in Fig. 3) and four “iso-normalized enthalpy” (n° 9, 10, 11, 12 in Fig. 3) parameter sets. The aim was to determine how the algorithm behaves if one parameter (speed, power, or normalized enthalpy) is constant for all parameter sets in the training database, and remains the same for the unseen parameter set. The confidence matrices in Table 9 show that for the three considered training sets, the classification accuracies are high (> 88%), despite the fact that only four parameter sets were used for the training.

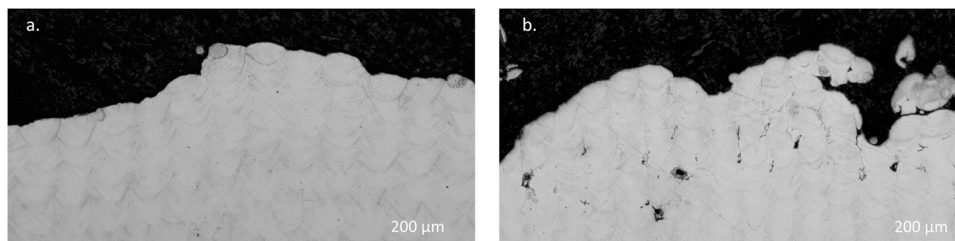


Fig. 8. Micrograph of a cross section of the sample. a) n°4 in the *conduction mode* domain and b) of the n°1 in the *LoF pores* domain. The parameter sets used for these samples are at the boundary between the *conduction mode* and *LoF pores* domains.

Table 6

Confusion matrices for CNN models trained with ten, eight, and six parameter sets and tested on the highest speed set, lowest speed set, highest power set, and lowest power set.

10 sets												
Highest speed				Lowest speed			Highest power			Lowest power		
Ground truth \ Classification accuracy [%]	Keyhole pores	Conduction mode	LoF pores	Keyhole pores	Conduction mode	LoF pores	Keyhole pores	Conduction mode	LoF pores	Keyhole pores	Conduction mode	LoF pores
Keyhole pores	88	17	4	93	1	4	91	9	4	95	1	3
Conduction mode	2	83	1	6	99	5	8	91	5	4	74	2
LoF pores	10	0	95	1	0	91	1	0	91	1	12	95

8 sets												
Highest speed				Lowest speed			Highest power			Lowest power		
Ground truth \ Classification accuracy [%]	Keyhole pores	Conduction mode	LoF pores	Keyhole pores	Conduction mode	LoF pores	Keyhole pores	Conduction mode	LoF pores	Keyhole pores	Conduction mode	LoF pores
Keyhole pores	100	3	1	93	0	3	94	11	2	94	5	0
Conduction mode	0	97	0	7	100	4	4	88	0	3	93	0
LoF pores	0	0	99	0	0	93	2	1	98	3	2	100

6 sets												
Highest speed				Lowest speed			Highest power			Lowest power		
Ground truth \ Classification accuracy [%]	Keyhole pores	Conduction mode	LoF pores	Keyhole pores	Conduction mode	LoF pores	Keyhole pores	Conduction mode	LoF pores	Keyhole pores	Conduction mode	LoF pores
Keyhole pores	78	16	3	83	2	16	91	13	7	92	7	4
Conduction mode	8	82	1	15	98	14	6	80	3	6	71	2
LoF pores	14	2	96	2	0	70	3	7	90	2	22	94

Table 7

The RMS “distance” values d_{p_RMS} (considering laser power) and d_{s_RMS} (considering laser speed) between the training parameter sets and the central unseen parameter set. The close parameter sets and distant ones are distinguished.

	d_{p_RMS} (W)	d_{s_RMS} (mm/s)
Distant training sets to the unseen set	12	61
Closest training sets to the unseen set	5	16

Additionally, for each process regime (*keyhole pores*, *conduction mode*, and *LoF pores*), the set with the highest power (n°1) was selected as the unseen parameter set, and the two sets with the lowest power values (n° 3 and 4) were used for the training database. The resulting classification accuracy was then compared with the one obtained with a training database made of the two sets with the smallest d_p to the unseen parameter set n°1 (i.e., n°2 and 13). The same procedure was applied considering the laser speed or the normalized enthalpy instead of the power. In the former case, the unseen parameter was chosen as n°8, and the CNN was either trained with the parameter sets n°5 & 6 or with the

Table 8

Confusion matrices for CNN models trained with the a. six closest parameter sets to the unseen central parameter set, and the b. six more distant points, for each regime.

a. Closest (i.e. full markers)				b. Furthest (i.e. empty markers)			
Ground truth \ Classification accuracy [%]	Keyhole pores	Conduction mode	LoF pores	Ground truth \ Classification accuracy [%]	Keyhole pores	Conduction mode	LoF pores
Keyhole pores	97	1	0	Keyhole pores	91	1	1
Conduction mode	2	98	1	Conduction mode	7	98	2
LoF pores	1	1	99	LoF pores	2	1	97

Table 9

Confusion matrices for CNN models predicting the process regime of an unseen 'central' parameter set, with one of the parameters being the same as the one in the training set. Three training databases made of 4 parameter sets were considered with a. iso-speed, b. iso-power, and c. iso-enthalpy.

a. Iso-speed				b. Iso-power			
Ground truth \ Classification accuracy [%]	Keyhole pores	Conduction mode	LoF pores	Ground truth \ Classification accuracy [%]	Keyhole pores	Conduction mode	LoF pores
Keyhole pores	88	3	2	Keyhole pores	96	4	0
Conduction mode	11	97	6	Conduction mode	2	93	1
LoF pores	1	0	92	LoF pores	2	3	99

c. Iso-enthalpy			
Ground truth \ Classification accuracy [%]	Keyhole pores	Conduction mode	LoF pores
Keyhole pores	93	1	3
Conduction mode	3	97	2
LoF pores	1	0	100

n°13 & 7. In the latter case, the unseen parameter was chosen as n°12, and the CNN was either trained with the parameter sets n°9 & 10 or with the n°11 & 13. The results are presented in [Table 10](#).

One can observe that the average classification accuracy is 18% higher when the training parameter sets are closer to the unseen parameter set in terms of laser speed (smaller d_s) and 5% higher when they are closer in terms of laser power (smaller d_p). The difference can be explained by the fact that, in the present DoE, the power range is smaller than the speed range. It can still be concluded that the smaller d_s and d_p , the higher would be the classification accuracies for the unseen

parameter set.

However, when comparing the influence of $d_{\Delta E}$, it can be seen that the accuracies are similar for both conditions (on average, 75% for a smaller $d_{\Delta E}$, and 78% for a higher $d_{\Delta E}$). [Table 11](#) presents the values of $d_{\Delta E}$ along with the corresponding values of d_s and d_p , for the predictions where the difference in $d_{\Delta E}$ is considered. While $d_{\Delta E}$ is higher for the sample in conduction mode, the corresponding d_s is equal to zero, which could explain that a higher classification accuracy (94% compared to 64%) is achieved, even though $d_{\Delta E}$ is higher. It can be presumed from these observations that the relative normalized distance in terms of

Table 10

Confusion matrices for CNN models trained on two parameter sets and used for predicting the process regime on an unseen condition with the highest power, speed or enthalpy values compared to the training parameter sets, distinguishing training databases with the smallest and highest d_s , d_p , and $d_{\Delta E}$ values.

Closest

Distance in speed				Distance in power			Distance in enthalpy		
Ground truth \ Classification accuracy [%]	Keyhole pores	Conduction mode	LoF pores	Keyhole pores	Conduction mode	LoF pores	Keyhole pores	Conduction mode	LoF pores
	88	21	18	85	9	10	80	25	15
	3	78	15	13	90	4	18	64	4
	9	1	67	2	1	86	2	11	81
Average				85			75		

Most distant

Distance in speed				Distance in power			Distance in enthalpy		
Ground truth \ Classification accuracy [%]	Keyhole pores	Conduction mode	LoF pores	Keyhole pores	Conduction mode	LoF pores	Keyhole pores	Conduction mode	LoF pores
	61	46	30	88	13	14	85	6	25
	9	52	3	10	87	13	14	94	18
	30	1	67	2	0	73	1	2	56
Average				82			78		

Table 11

Values of d_s , d_p , and $d_{\Delta E}$ when predicting the process regime of an unseen condition with the lowest and the highest $d_{\Delta E}$.

	d_s [%]		d_p [%]		$d_{\Delta E}$ [%]	
	Closest	Most distant	Closest	Most distant	Closest	Most distant
Keyhole pores	21	31.6	8.6	6.6	3	28.6
Conduction mode	6	0	15.7	39.8	12.5	40
LoF pores	6	5.3	8.5	18	5.5	22

normalized enthalpy is not a very relevant parameter.

3.2.4. Relative normalized distance in terms of power and speed

All the aforementioned CNN prediction results motivate an in-depth investigation of the influence of the number of parameter sets and the relative normalized distance in terms of power and speed (d_p and d_s) on the robustness of the model's performance. Several models were trained with various numbers of parameter sets (from two to twelve), with different relative positions of the training sets with respect to the unseen parameter set, and with different values of d_p and d_s . The resulting classification accuracies were averaged between the three process regimes (keyhole pores, conduction mode, and LoF pores). Fig. 9 and Fig. 10

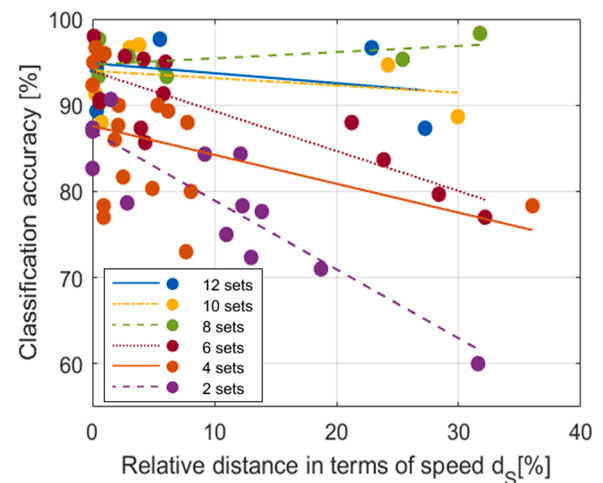


Fig. 9. Average classification accuracy of the processing regime of the unseen parameter set, as a function of the relative normalized distance in terms of speed d_s for different numbers of parameter sets included in the training database (from 2 to 12).

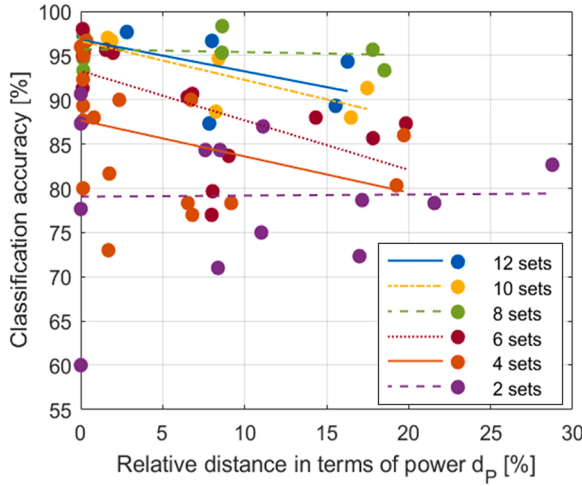


Fig. 10. Average classification accuracy of the processing regime of the unseen parameter set, as a function of the relative normalized distance in terms of power d_p for different numbers of parameter sets included in the training database (from 2 to 12).

present the average classification accuracy for the unseen parameter sets as a function of the relative normalized distance in terms of speed (d_s) and power (d_p), respectively, for the different numbers of training sets used in the CNN database. The linear regressions of accuracies, obtained with a common number of training sets, are plotted in dotted lines (Fig. 9 and Fig. 10) in order to highlight tendencies.

It can be first observed that the higher the number of parameter sets included in the training database, the higher the average classification accuracy. Additionally, a general trend can be highlighted: the higher the relative normalized distance (for both d_p and d_s), the lower the classification accuracies. One outlier is the prediction of the sample n°4 regime (conduction mode), when using 10 and 12 training sets. The processing conditions refer, as aforementioned, to the intersection between the *conduction mode* domain and the *LoF pores* domain. In the context of predicting processing maps, and as already noted, this feature is interesting, as it indicates a transition zone between 2 process regimes. When eight parameters are included in the database, the prediction for this condition n°4 has a higher accuracy (93%), which explains the excellent average results with 8 training sets, even better than those with 10 or 12 training sets. The relatively scattered nature of the results can be explained by the statistical behavior of the CNN.

Nevertheless, if at least eight parameter sets compose the training database, the resulting model seems to be robust and able to predict with high confidence (>88%) the entire studied processing map, regardless of the distance in terms of speed and power (up to a difference of approximately 30%). When training with only two parameter sets, the results are very scattered and seem more related to the process parameters differences (power and speed) than to the laser-material interaction. In other words, using only two training sets is not enough to have a reliable model.

In order to compare the influence of the relative normalized distance in power and the relative normalized distance in speed, Fig. 11 presents the linear regressions of all results displayed in Fig. 9 and Fig. 10, when at least four parameter sets were included in the training database, and distinguishing between the two types of distance. The systematically larger slopes of accuracies as a function of d_p point towards a bigger influence of the relative normalized distance in power. The difference in slope between the two considered linear regressions (as a function of d_s and d_p) varies significantly depending on the number of training parameter sets (from 17% with 4 and 6 parameter sets up to 80% with 10 parameter sets). Although the influence of d_p appears somehow larger, both d_s and d_p should be minimized to guarantee high classification

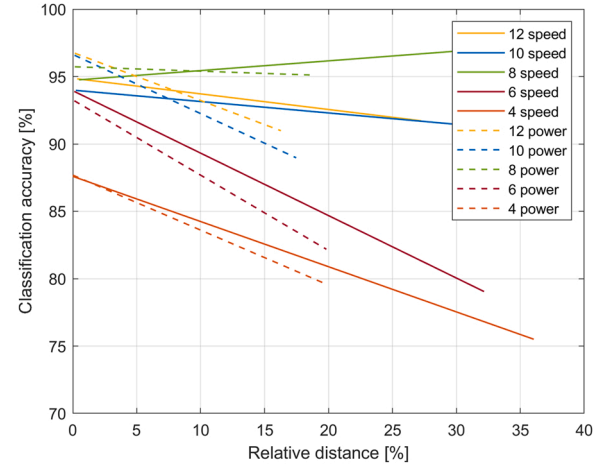


Fig. 11. Linear regressions of the average classification accuracy when predicting the process regime of an unseen parameter set as a function of the distance d_s (speed) and d_p (power).

accuracies.

4. Conclusions

This work presents the results of a CNN model applied to spectrograms extracted from measurements of an airborne acoustic sensor for the classification of LPBF processing regimes. The microphone placed inside a custom-design LPBF machined recorded the acoustic signals of the process for 39 different process parameters, i.e., thirteen parameter sets per process regime (*keyhole pores*, *conduction mode*, or *LoF pores*). The labeling of the categories for each process condition was verified by cross-section analysis. A CNN model was optimized for spectrograms extracted from the acoustic signals filtered with a low pass filter at 60 kHz, downsampled 4 times, and normalized.

The aim of this contribution was to establish a methodology for the construction of a robust training database, leading to a CNN able to predict the processing regime in conditions unseen in the database, covering the entire LPBF processing map of 316 L steel. The three considered regimes are *LoF pores*, *conduction mode*, and *keyhole pores*. The CNN model is trained on a given number of laser parameter sets and used for predicting the process regime of an unseen parameter set. The resulting classification accuracy is very high (>97%), proving that it is possible to construct a model general enough to identify the features related to specific laser-material interactions and leading to specific metallurgical states. Three main parameters are found to influence the classification accuracy. The first one is the relative normalized distance in terms of power and speed between the average laser parameters used in the training sets and those of the unseen parameter set (d_s , d_p). The second is the number of parameter sets included in the training database, and the third is the position (in the processing map) of the training sets relative to that of the unseen parameter set. These three parameters have been proven to be interdependent. Results highlight that higher d_s and d_p values lower the classification accuracies. The influence of the relative normalized distance in terms of normalized enthalpy $d_{\Delta E}$ does not seem to be relevant. However, the influence of d_p seems to be higher than that of d_s . Moreover, it has been concluded that, on average, the higher the number of parameter sets in the training database, the higher the classification accuracy. Two parameter sets are not enough to allow a model to generalize. A minimum number of eight training sets is identified, leading to high classification accuracies (>88%) for all relative normalized distances and positions considered in the present DoE. This number can be lowered to six if the training sets surrounding the unseen parameter set have a d_s and d_p lower than 5%. If one process parameter (speed, power, or normalized enthalpy) is constant among all

sets in the training database and common to the unseen parameter set, then four training sets are enough for predicting the process regime with high accuracy, regardless of the particular choice of process parameters.

In summary, one model trained with eight distinct laser parameter sets randomly distributed in each process regime domain would be sufficient to classify the entire processing map. Once a robust model is obtained, a decrease in the classification accuracy can help identify the boundaries between different domains in the 2D processing map. This can significantly facilitate the time-consuming building of an LPBF processing map for a given alloy. In the context of in-situ acoustic monitoring for the control of the LPBF process, we demonstrate here that unexpected processing conditions happening during the fabrication of a 3D part could be detected, for example, by predicting from the AE signals a regime different from the conduction mode. In future work, the understanding of the features and frequencies responsible for specific laser material interactions, in each process regime, will be investigated based on the present results. The same methodology could be applied to the detection of other various critical events, such as crack propagation or microstructure changes.

Funding

The authors would like to acknowledge the financial support of the project MoCont from the program of the Strategic Focus Area in Advanced Manufacturing (SFA-AM), a strategic initiative of the ETH Board.

CRedit authorship contribution statement

Charlotte de Formanoir: Writing – review & editing, Supervision, Methodology. **Kilian Wasmer:** Writing – review & editing, Supervision, Funding acquisition. **Daoudi Rita Drissi:** Writing – original draft, Methodology, Investigation, Formal analysis, Data curation, Conceptualization. **Giulio Masinelli:** Writing – review & editing, Validation, Software. **Jamasp Jhabvala:** Resources. **Roland Logé:** Writing – review & editing, Supervision, Project administration, Methodology, Funding acquisition.

Data Availability

Data will be made available on request.

Acknowledgment

The members of LMTM gratefully acknowledge the generous sponsoring of PX Group to their laboratory.

Disclosure statement

The authors declare no conflict of interest.

Appendix A. Supporting information

Supplementary data associated with this article can be found in the online version at [doi:10.1016/j.addma.2023.103484](https://doi.org/10.1016/j.addma.2023.103484).

References

- [1] T. DebRoy, et al., Additive manufacturing of metallic components – process, structure and properties, *Prog. Mater. Sci.* vol. 92 (2018) 112–224, <https://doi.org/10.1016/j.pmatsci.2017.10.001>.
- [2] N.K. Dey, Additive manufacturing laser deposition of Ti-6Al-4V for aerospace repair application, p. 70.
- [3] K. Zeng, D. Pal, and B. Stucker, A review of thermal analysis methods in Laser Sintering and Selective Laser Melting, p. 19.
- [4] R. Liu, Z. Wang, T. Sparks, F. Liou, J. Newkirk, Aerospace applications of laser additive manufacturing, *Laser Addit. Manuf. Mater. Des. Technol. Appl.* (2016) 351–371, <https://doi.org/10.1016/B978-0-08-100433-3.00013-0>.
- [5] J.M. Williams, et al., Bone tissue engineering using polycaprolactone scaffolds fabricated via selective laser sintering, *Biomaterials* vol. 26 (23) (2005) 4817–4827, <https://doi.org/10.1016/j.biomaterials.2004.11.057>.
- [6] J. Gao, J. Folkes, O. Yilmaz, N. Gindy, Investigation of a 3D non-contact measurement based blade repair integration system, *Aircr. Eng. Aerosp. Technol.* vol. 77 (2005) 34–41, <https://doi.org/10.1108/00022660510576028>.
- [7] C.L. Ventola, Medical applications for 3D printing: current and projected uses, *P T Peer-Rev. J. Formul. Manag.* vol. 39 (10) (2014) 704–711.
- [8] B. Vandenbroucke, J. Kruth, Selective laser melting of biocompatible metals for rapid manufacturing of medical parts, *Rapid Prototyp. J.* vol. 13 (4) (2007) 196–203, <https://doi.org/10.1108/13552540710776142>.
- [9] A. Mostafaei, et al., Defects and anomalies in powder bed fusion metal additive manufacturing, *Curr. Opin. Solid State Mater. Sci.* vol. 26 (2) (2022), <https://doi.org/10.1016/j.cossms.2021.100974>.
- [10] M. Montazeri, R. Yavari, P. Rao, P. Boulware, In-process monitoring of material cross-contamination defects in laser powder bed fusion, *J. Manuf. Sci. Eng.* vol. 140 (11) (2018), <https://doi.org/10.1115/1.4040543>.
- [11] P. Hanzl, M. Zetek, T. Bakša, T. Kroupa, The influence of processing parameters on the mechanical properties of SLM parts, *Procedia Eng.* vol. 100 (2015) 1405–1413, <https://doi.org/10.1016/j.proeng.2015.01.510>.
- [12] A. Ramalho, T.G. Santos, B. Bevens, Z. Sinoqi, P. Rao, J.P. Oliveira, Effect of contaminations on the acoustic emissions during wire and arc additive manufacturing of 316L stainless steel, *Addit. Manuf.* vol. 51 (2022), 102585, <https://doi.org/10.1016/j.addma.2021.102585>.
- [13] W. King, et al., Laser powder bed fusion additive manufacturing of metals; physics, computational, and materials challenges, *Appl. Phys. Rev.* vol. 2 (2015), 041304, <https://doi.org/10.1063/1.4937809>.
- [14] T. Mukherjee, T. DebRoy, Mitigation of lack of fusion defects in powder bed fusion additive manufacturing, *J. Manuf. Process.* vol. 36 (2018) 442–449, <https://doi.org/10.1016/j.jmapro.2018.10.028>.
- [15] M. Tang, P.C. Pistorius, J.L. Beuth, Prediction of lack-of-fusion porosity for powder bed fusion, *Addit. Manuf.* vol. 14 (2017) 39–48, <https://doi.org/10.1016/j.addma.2016.12.001>.
- [16] K. Darvish, Z.W. Chen, T. Pasang, Reducing lack of fusion during selective laser melting of CoCrMo alloy: effect of laser power on geometrical features of tracks, *Mater. Des.* vol. 112 (2016) 357–366, <https://doi.org/10.1016/j.matdes.2016.09.086>.
- [17] M. Laleh, et al., Two and three-dimensional characterisation of localised corrosion affected by lack-of-fusion pores in 316L stainless steel produced by selective laser melting, *Corros. Sci.* vol. 165 (2020), 108394, <https://doi.org/10.1016/j.corsci.2019.108394>.
- [18] C. Zhao, et al., Critical instability at moving keyhole tip generates porosity in laser melting, *Science* vol. 370 (6520) (2020) 1080–1086, <https://doi.org/10.1126/science.abd1587>.
- [19] A.A. Martin, et al., Dynamics of pore formation during laser powder bed fusion additive manufacturing, *Nat. Commun.* vol. 10 (1) (2019) 1987, <https://doi.org/10.1038/s41467-019-10009-2>.
- [20] F. Lu, X. Li, Z. Li, X. Tang, H. Cui, Formation and influence mechanism of keyhole-induced porosity in deep-penetration laser welding based on 3D transient modeling, *Int. J. Heat. Mass Transf.* vol. 90 (2015) 1143–1152, <https://doi.org/10.1016/j.ijheatmasstransfer.2015.07.041>.
- [21] W.E. King, et al., Observation of keyhole-mode laser melting in laser powder-bed fusion additive manufacturing, *J. Mater. Process. Technol.* vol. 214 (12) (2014), <https://doi.org/10.1016/j.jmatprotec.2014.06.005>.
- [22] T. Klein, M. Vicanek, J. Kroos, I. Decker, G. Simon, Oscillations of the keyhole in penetration laser beam welding, *J. Phys. Appl. Phys.* vol. 27 (10) (1994) 2023–2030, <https://doi.org/10.1088/0022-3727/27/10/006>.
- [23] T. Qi, H. Zhu, H. Zhang, J. Yin, L. Ke, X. Zeng, Selective laser melting of Al7050 powder: melting mode transition and comparison of the characteristics between the keyhole and conduction mode, *Mater. Des.* vol. 135 (2017), <https://doi.org/10.1016/j.matdes.2017.09.014>.
- [24] H. Ghasemi-Tabasi, J. Jhabvala, E. Boillat, T. Ivas, R. Drissi-Daoudi, R.E. Logé, An effective rule for translating optimal selective laser melting processing parameters from one material to another, *Addit. Manuf.* vol. 36 (2020), 101496, <https://doi.org/10.1016/j.addma.2020.101496>.
- [25] W.M. Tucho, V.H. Lysne, H. Austbø, A. Sjolyst-Kverneland, V. Hansen, Investigation of effects of process parameters on microstructure and hardness of SLM manufactured SS316L, *J. Alloy. Compd.* vol. 740 (2018) 910–925, <https://doi.org/10.1016/j.jallcom.2018.01.098>.
- [26] I. Koutiri, E. Pessard, P. Peyre, O. Amlou, T. De Terris, Influence of SLM process parameters on the surface finish, porosity rate and fatigue behavior of as-built Inconel 625 parts, *J. Mater. Process. Technol.* vol. 255 (2018) 536–546, <https://doi.org/10.1016/j.jmatprotec.2017.12.043>.
- [27] T. Mishurova, K. Artzt, J. Haubrich, G. Requena, G. Bruno, New aspects about the search for the most relevant parameters optimizing SLM materials, *Addit. Manuf.* vol. 25 (2019) 325–334, <https://doi.org/10.1016/j.addma.2018.11.023>.
- [28] Y.H. Zhou, et al., Selective laser melting of typical metallic materials: an effective process prediction model developed by energy absorption and consumption analysis, *Addit. Manuf.* vol. 25 (2019) 204–217, <https://doi.org/10.1016/j.addma.2018.10.046>.
- [29] R. Drissi-Daoudi, et al., Differentiation of materials and laser powder bed fusion processing regimes from airborne acoustic emission combined with machine learning, *Virtual Phys. Prototyp.* vol. 17 (2) (2022) 181–204, <https://doi.org/10.1080/17452759.2022.2028380>.
- [30] V. Gunenthiram, P. Peyre, M. Schneider, M. Dal, C. Frederic, R. Fabbro, Analysis of laser-melt pool-powder bed interaction during the selective laser melting of a

- stainless steel, *J. Laser Appl.* vol. 29 (2017), 022303, <https://doi.org/10.2351/1.4983259>.
- [31] M.J. Matthews, G. Guss, S.A. Khairallah, A.M. Rubenchik, P.J. Depond, W.E. King, Denudation of metal powder layers in laser powder bed fusion processes, *Acta Mater.* vol. 114 (2016) 33–42, <https://doi.org/10.1016/j.actamat.2016.05.017>.
- [32] V. Gunenthiram, et al., Experimental analysis of spatter generation and melt-pool behavior during the powder bed laser beam melting process, *J. Mater. Process. Technol.* vol. 251 (2018) 376–386, <https://doi.org/10.1016/j.jmatprotec.2017.08.012>.
- [33] P. Bidare, I. Bitharas, R.M. Ward, M.M. Attallah, A.J. Moore, Fluid and particle dynamics in laser powder bed fusion, *Acta Mater.* vol. 142 (2018) 107–120, <https://doi.org/10.1016/j.actamat.2017.09.051>.
- [34] S.A. Khairallah, A.T. Anderson, A. Rubenchik, W.E. King, Laser powder-bed fusion additive manufacturing: physics of complex melt flow and formation mechanisms of pores, spatter, and denudation zones, *Acta Mater.* vol. 108 (2016) 36–45, <https://doi.org/10.1016/j.actamat.2016.02.014>.
- [35] D. Wang, et al., Mechanisms and characteristics of spatter generation in SLM processing and its effect on the properties, *Mater. Des.* vol. 117 (2017) 121–130, <https://doi.org/10.1016/j.matdes.2016.12.060>.
- [36] S. Berumen, F. Bechmann, S. Lindner, J.P. Kruth, T. Craeghs, Quality control of laser- and powder bed-based Additive Manufacturing (AM) technologies, *Phys. Procedia* vol. 5 (PART 2) (2010) 617–622, <https://doi.org/10.1016/j.phpro.2010.08.089>.
- [37] S. Clijsters, T. Craeghs, S. Buls, K. Kempen, J.P. Kruth, In situ quality control of the selective laser melting process using a high-speed, real-time melt pool monitoring system, *Int. J. Adv. Manuf. Technol.* vol. 75 (5–8) (2014) 1089–1101, <https://doi.org/10.1007/s00170-014-6214-8>.
- [38] S. Shevchik, et al., Supervised deep learning for real-time quality monitoring of laser welding with X-ray radiographic guidance, *Sci. Rep.* vol. 10 (1) (2020) 3389, <https://doi.org/10.1038/s41598-020-60294-x>.
- [39] M. Pavlov, M. Doubenskaia, I. Smurov, Pyrometric analysis of thermal processes in SLM technology, *Phys. Procedia* vol. 5 (2010) 523–531, <https://doi.org/10.1016/J.PHPRO.2010.08.080>.
- [40] M. Doubenskaia, M. Pavlov, Y. Chivel, Optical system for on-line monitoring and temperature control in selective laser melting technology, *Key Eng. Mater.* vol. 437 (2010) 458–461, <https://doi.org/10.4028/www.scientific.net/KEM.437.458>.
- [41] T. Furumoto, T. Ueda, M.R. Alkahari, A. Hosokawa, Investigation of laser consolidation process for metal powder by two-color pyrometer and high-speed video camera, *CIRP Ann.* vol. 62 (1) (2013) 223–226, <https://doi.org/10.1016/J.CIRP.2013.03.032>.
- [42] J.-B. Forien, N.P. Calt, P.J. Depond, G.M. Guss, T.T. Roehling, M.J. Matthews, Detecting keyhole pore defects and monitoring process signatures during laser powder bed fusion: a correlation between in situ pyrometry and ex situ X-ray radiography, *Addit. Manuf.* vol. 101336 (2020).
- [43] A. Gaikwad, B. Giera, G.M. Guss, J.B. Forien, M.J. Matthews, P. Rao, Heterogeneous sensing and scientific machine learning for quality assurance in laser powder bed fusion – a single-track study, *Addit. Manuf.* vol. 36 (2020), 101659, <https://doi.org/10.1016/j.addma.2020.101659>.
- [44] T. Furumoto, M.R. Alkahari, T. Ueda, M.S.A. Aziz, A. Hosokawa, Monitoring of laser consolidation process of metal powder with high speed video camera, *Phys. Procedia* vol. 39 (2012) 760–766, <https://doi.org/10.1016/J.PHPRO.2012.10.098>.
- [45] L. Li, W.M. Steen, Non-contact acoustic emission monitoring during laser processing, *LIA Laser Inst. Am.* vol. 75 (1993) 719–728, <https://doi.org/10.2351/1.5058543>.
- [46] Y. Mao, G. Kinsman, W.W. Duley, Real-time fast fourier transform analysis of acoustic emission during CO₂ laser welding of materials, *J. Laser Appl.* vol. 5 (2) (1993) 17–22, <https://doi.org/10.2351/1.4745326>.
- [47] W.W. Duley, Y.L. Mao, The effect of surface condition on acoustic emission during welding of aluminium with CO₂ laser radiation, *J. Phys. Appl. Phys.* vol. 27 (7) (1994) 1379–1383, <https://doi.org/10.1088/0022-3727/27/7/007>.
- [48] D. Farson, K. Hillsley, J. Sames, Frequency–time characteristics of air-borne signals from laser welds, *J. Laser Appl.* vol. 8 (1996) 33–42.
- [49] K. Wasmer, C. Kenel, C. Leinenbach, S.A. Shevchik, In situ and real-time Monitoring of Powder-Bed AM by combining acoustic emission and artificial intelligence, in *Industrializing additive manufacturing - proceedings of additive manufacturing in products and applications - AMPA2017*, Cham (2018) 200–209, https://doi.org/10.1007/978-3-319-66866-6_20.
- [50] S.A. Shevchik, et al., Laser welding quality monitoring via graph support vector machine with data adaptive kernel, *IEEE Access* vol. 7 (2019) 93108–93122, <https://doi.org/10.1109/ACCESS.2019.2927661>.
- [51] T. Le-Quang, et al., Why is in situ quality control of laser keyhole welding a real challenge? *Procedia CIRP* vol. 74 (2018) 649–653, <https://doi.org/10.1016/j.procir.2018.08.055>.
- [52] K. Wasmer, et al., Laser processing quality monitoring by combining acoustic emission and machine learning: a high-speed X-ray imaging approach, *Procedia CIRP* vol. 74 (2018) 654–658, <https://doi.org/10.1016/j.procir.2018.08.054>.
- [53] W. Huang, R. Kovacevic, A neural network and multiple regression method for the characterization of the depth of weld penetration in laser welding based on acoustic signatures, *J. Intell. Manuf.* vol. 22 (2) (2011) 131–143, <https://doi.org/10.1007/s10845-009-0267-9>.
- [54] H. Gu, W.W. Duley, A statistical approach to acoustic monitoring of laser welding, *J. Phys. Appl. Phys.* vol. 29 (3) (1996) 556–560, <https://doi.org/10.1088/0022-3727/29/3/011>.
- [55] S. Lee, S. Ahn, C. Park, Analysis of acoustic emission signals during laser spot welding of SS304 stainless steel, *J. Mater. Eng. Perform.* vol. 23 (3) (2014) 700–707, <https://doi.org/10.1007/s11665-013-0791-9>.
- [56] S.A. Shevchik, C. Kenel, C. Leinenbach, K. Wasmer, Acoustic emission for in situ quality monitoring in additive manufacturing using spectral convolutional neural networks, *Addit. Manuf.* vol. 21 (2018) 598–604, <https://doi.org/10.1016/j.addma.2017.11.012>.
- [57] L.W. Koester, H. Taheri, L.J. Bond, E.J. Faierson, Acoustic monitoring of additive manufacturing for damage and process condition determination, *AIP Conf. Proc.* vol. 2102 (1) (2019), 020005, <https://doi.org/10.1063/1.5099709>.
- [58] K. Ito, M. Kusano, M. Demura, M. Watanabe, Detection and location of microdefects during selective laser melting by wireless acoustic emission measurement, *Addit. Manuf.* vol. 40 (2021), 101915, <https://doi.org/10.1016/j.addma.2021.101915>.
- [59] H. Taheri, L.W. Koester, T.A. Bigelow, E.J. Faierson, L.J. Bond, In situ additive manufacturing process monitoring with an acoustic technique: clustering performance evaluation using k-means algorithm, *J. Manuf. Sci. Eng.* vol. 141 (4) (2019), <https://doi.org/10.1115/1.4042786>.
- [60] G. Masinelli, S.A. Shevchik, V. Pandiyan, T. Quang-Le, K. Wasmer, Artificial intelligence for monitoring and control of metal additive manufacturing in industrializing additive manufacturing, *Cham* (2021) 205–220, https://doi.org/10.1007/978-3-030-54334-1_15.
- [61] N. Eschner, L. Weiser, B. Häfner, G. Lanza, Classification of specimen density in Laser Powder Bed Fusion (L-PBF) using in-process structure-borne acoustic process emissions, *Addit. Manuf.* vol. 34 (2020), 101324, <https://doi.org/10.1016/j.addma.2020.101324>.
- [62] S.A. Shevchik, G. Masinelli, C. Kenel, C. Leinenbach, K. Wasmer, Deep learning for in situ and real-time quality monitoring in additive manufacturing using acoustic emission, *IEEE Trans. Ind. Inform.* vol. 15 (9) (2019) 5194–5203, <https://doi.org/10.1109/TII.2019.2910524>.
- [63] D. Ye, G.S. Hong, Y. Zhang, K. Zhu, J.Y.H. Fuh, Defect detection in selective laser melting technology by acoustic signals with deep belief networks, *Int. J. Adv. Manuf. Technol.* vol. 96 (5) (2018) 2791–2801, <https://doi.org/10.1007/s00170-018-1728-0>.
- [64] J.R. Tempelman, et al., Detection of keyhole pore formations in laser powder-bed fusion using acoustic process monitoring measurements, *Addit. Manuf.* vol. 55 (2022), 102735, <https://doi.org/10.1016/j.addma.2022.102735>.
- [65] K. Wasmer, T. Le-Quang, B. Meylan, S.A. Shevchik, In situ quality monitoring in AM using acoustic emission: a reinforcement learning approach, *J. Mater. Eng. Perform.* vol. 28 (2) (2019) 666–672, <https://doi.org/10.1007/s11665-018-3690-2>.
- [66] V. Pandiyan, et al., Semi-supervised monitoring of Laser powder bed fusion process based on acoustic emissions, *Virtual Phys. Prototyp.* vol. 16 (4) (2021) 481–497, <https://doi.org/10.1080/17452759.2021.1966166>.
- [67] V. Pandiyan, et al., Deep transfer learning of additive manufacturing mechanisms across materials in metal-based laser powder bed fusion process, *J. Mater. Process. Technol.* vol. 303 (2022), 117531, <https://doi.org/10.1016/j.jmatprotec.2022.117531>.
- [68] A.J. Jerri, The Shannon sampling theorem - its various extensions and applications: a tutorial review, *IEEE Proc.* vol. 65 (1977) 1565–1596.
- [69] D.B. Hann, J. Jammi, J. Folkes, A simple methodology for predicting laser-weld properties from material and laser parameters, *J. Phys. Appl. Phys.* vol. 44 (44) (2011), 445401, <https://doi.org/10.1088/0022-3727/44/44/445401>.
- [70] C.S. Kim, Thermophysical properties of stainless steels, United States, 1975.
- [71] K. Gutknecht, M. Cloots, R. Sommerhuber, K. Wegener, Mutual comparison of acoustic, pyrometric and thermographic laser powder bed fusion monitoring, *Mater. Des.* vol. 210 (2021), 110036, <https://doi.org/10.1016/j.matdes.2021.110036>.